A bio-optical model for integration into ecosystem models for the Ligurian Sea

Fethi Bengil[1*], David McKee[2], Sükrü T. Beşiktepe[3], Violeta Sanjuan Calzado[4], and Charles Trees[4].

[1] Marine School - Earth System Science Research Centre. Girne American University, University Drive, Girne, TRNC via Mersin 10 Turkey

[2] Physics Department, University of Strathclyde, 107 Rottenrow, Glasgow, G4 0NG, Scotland

[3] Institute of Marine Sciences and Technology, Dokuz Eylül University, Bakü Bulv. No:100, 35100, İnciraltı, İzmir Turkey

[4]Centre for Maritime Research and Experimentation, 400 Viale San Bartolomeo, 19126La Spezia (SP), Italy

Corresponding author. E-mail address: fethibengil@gau.edu.tr.

Keywords: Bio-optical model, Ligurian Sea, ocean colour, photosynthetically available radiation

Abstract:

A bio-optical model has been developed for the Ligurian Sea which encompasses both deep, oceanic Case 1 waters and shallow, coastal Case 2 waters. The model builds on earlier Case 1 models for the region and uses field data collected on the BP09 research cruise to establish new relationships for non-biogenic particles and CDOM. The bio-optical model reproduces *in situ* IOPs accurately and is used to parameterize radiative transfer simulations which demonstrate its utility for modeling underwater light levels and above surface remote sensing reflectance. Prediction of euphotic depth is found to be accurate to within ~3.2 m (RMSE). Previously

26 published light field models work well for deep oceanic parts of the Ligurian Sea that fit the
27 Case 1 classification. However, they are found to significantly over-estimate euphotic depth in
28 optically complex coastal waters where the influence of non-biogenic materials is strongest.
29 For these coastal waters, the combination of the bio-optical model proposed here and full
30 radiative transfer simulations provides significantly more accurate predictions of euphotic
31 depth.
32
33 **1. Introduction**
34 The temporal and spatial variability of oceanic optical properties are fundamental to
35 many biogeochemical processes in the sea (Dickey and Falkowski 2002). Underwater light
36 fields regulate photosynthesis, contribute to solar heating and determine remotely sensed ocean
37 colour signals. In recent years it has become increasingly apparent that coupled physical-
38 ecosystem models require appropriate representation of the underwater light field, particularly
39 in the context of using ocean colour remote sensing data for assimilation and validation
40 (Rothstein *et al.* 2006, Dickey *et al.* 2006, Fujii *et al.* 2007). Advances in computing power
41 and availability of fast and accurate radiative transfer models (e.g. Ecolight, Sequoia Scientific)
42 offer the potential to incorporate comprehensive light field models into aquatic ecosystem
43 models, with the promise of significant improvements in the prediction of biogeochemical and
44 physical properties (Mobley *et al.* 2015).
45 Early attempts to integrate light field models into coupled ecosystem models tended to
46 use very basic approaches to modeling the underwater light field. For example, Beşiktepe *et*
47 *al.* (2003) used chlorophyll concentration (*Chl*) and the Lambert-Beer law to obtain attenuation
48 coefficients and from this estimated underwater light fields. Penta et al. (2008 and 2009)
49 adapted the innovative method of Lee et al. (2005) to obtain underwater light attenuation for
50 marine ecosystem models. Recent studies have adopted more sophisticated approaches to

model underwater light fields (e.g. Fujii *et al.* 2007, Shulman *et al.* 2013, Ciavatta *et al.* 2014). Future efforts, incorporating full solution of the radiative transfer equation, will require parameterization with a complete set of inherent optical properties, *IOPs* (Trees *et al.* 2009). Moreover, there will be a need to relate these IOPs to relevant ecosystem model currencies in order to track evolution of the light field in time and space with changes in physical and biogeochemical properties of the system. Considerable effort has already gone into the development of bio-optical models for different natural water systems (Prieur and Sathyendranath 1981, Gordon and Morel 1981, Morel 1988, Bricaud *et al.* 1995, Bricaud *et al.* 1998, Loisel and Morel 1998, Morel and Maritorena 2001, Velluci 2007, and Morel 2009).

Most bio-optical models are constructed using optically significant constituents (*OSC*) as currency terms, with typical components such as: phytoplankton, detrital or non-algal particles and coloured dissolved organic material (*CDOM*). Even such a simple scheme presents difficulties in terms of relating optical variables to parameters that can be included in an ecosystem model currency scheme. Phytoplankton is the least awkward component, usually being represented by chlorophyll concentration as a proxy currency. The remainder of the particle population is much harder to define. In oceanic systems, operating under the Case 1 definition, other particles may be assumed to be derived from the phytoplankton population, e.g. detrital particles and associated bacterial populations, and these might also be related to *Chl*. However, in shallow coastal waters there is also the potential for significant populations of non-biogenic particles from terrigenous sources or from benthic resuspension. These particles are unlikely to be related to *Chl* and must, instead, be represented by some measure of total suspended solid concentration (*TSS*). However, given the contribution from phytoplankton and associated biogenic materials to *TSS*, there is an *a priori* requirement for consideration of further refinement of this parameterization to account for the complex nature of the particle population. *CDOM* is also problematic when considering Case 1 versus Case 2

76 scenarios. Under the Case 1 approach, *CDOM* is assumed to be a product of algal-related
77 biological activity and has been successfully related to *Chl* for oceanic waters (Prieur &
78 Sathyendranath 1981, Bricaud *et al.* 1998). However, coastal areas subject to riverine inputs
79 will present *CDOM* signals that are unrelated to *Chl*. Here there are grounds for investigating
80 the potential of relating *CDOM* signals to salinity given the association with freshwater inputs
81 (e.g. Bowers *et al.* 2008 and references therein).

82 The study area for this paper is the Ligurian Sea, which is located in the northwestern
83 part of the Mediterranean Sea between southeast France, northwest Italy and the island of
84 Corsica (Figure 1). This is an area which has been extensively studied previously with well-
85 established circulation patterns, e.g. Astraldi & Gasparini (1992). Cyclonic circulation in the
86 Ligurian Sea leads to the formation of three distinct hydrological zones; a thermal front (frontal
87 zone) which separates less dense warm coastal peripheral water (coastal zone) from denser cold
88 offshore water (central zone) (Picco *et al.* 2010 and references therein). These structures are
89 permanent but show some seasonal and interannual variability (Astraldi *et al.* 1990, Picco *et*
90 *al.* 2010). The upper layer of the Ligurian Sea has seasonal differences in nutrient ratios with
91 changes from nitrate limitation in winter to phosphate limitation in summer due to seasonal
92 hydrological regime variations (Marty *et al.* 2002). Nutrient availability is controlled by
93 vertical mixing and determines the timing of algal blooms. Winter mixing leads to the
94 formation of a winter – early spring bloom while a second bloom in April – May depends on
95 subsequent mixing events (Raick *et al.* 2005).

96 The aim of this study is to develop and test a bio-optical model for the Ligurian Sea,
97 which uses *Chl*, *TSS* and *Salinity* as the currency exchange with an ecosystem model, based
98 upon derivation of appropriate mass-specific inherent optical properties with different versions
99 for deep offshore waters and shallow, optically complex coastal waters. This is an important
100 step for establishing a conceptual framework to integrate a robust bio-optical model into future

coupled physical-ecosystem models for this region. The choice of *OSC* currency parameters (*Chl*, *TSS* and *Salinity*) reflects parameters that could be obtained both from autonomous *in situ* sensor systems and from ecosystem model outputs. *Chl* and *TSS* may also be derived from ocean colour remote sensing, whilst salinity can be obtained from microwave remote sensing e.g. Aquarius and SMOS (Klemas 2011).

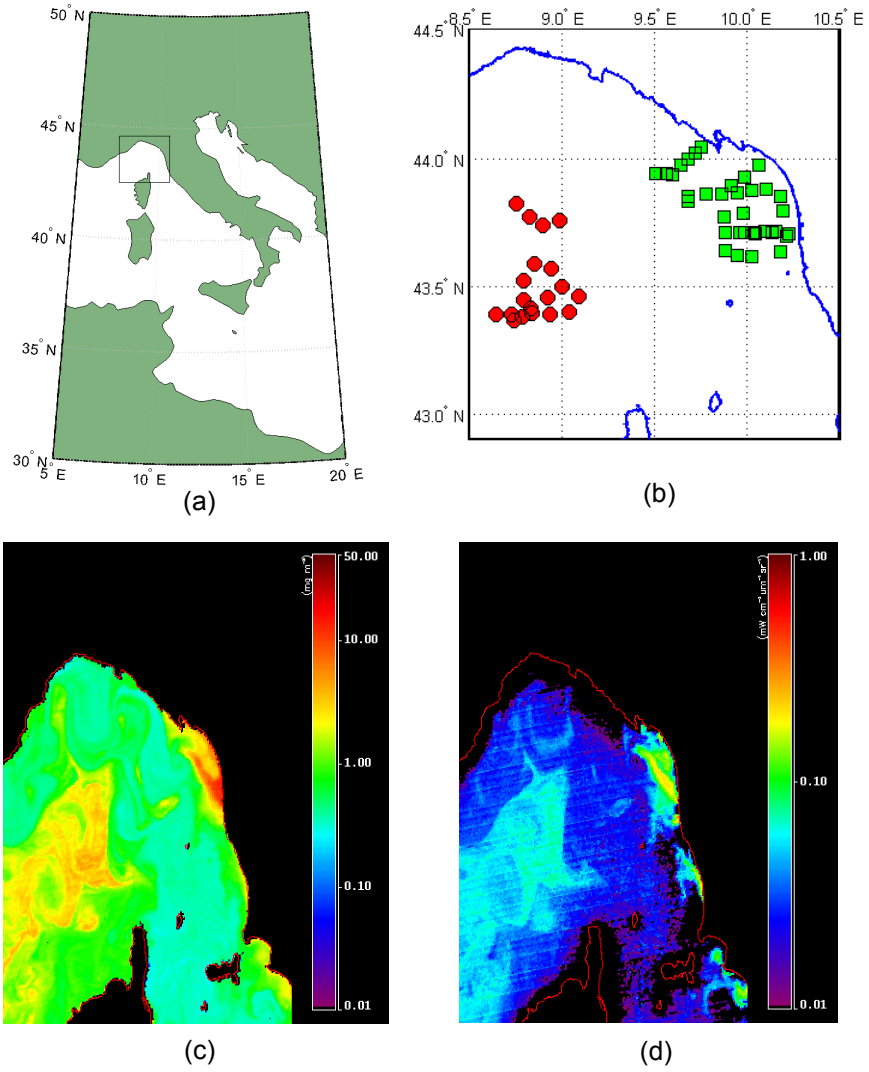

Figure 1. (a) Study area and (b) location of offshore (circles) and onshore (squares) stations for the BP09 cruise. (c) MODIS standard *Chl* from 18th March 2009 shows a bloom in the central region of the Ligurian Sea, northwest of Corsica. The high intensity "bloom" on the Italian coast is actually a sediment plume from the River Arno, which is clearly identified from (d) MODIS *nLw667* from the same date.

2. Material and Methods

2.1 Data

The data used in this study were collected during the BP09 Cruise between March 13th and 26th 2009 in the Ligurian Sea on board *NR/V Alliance*. Figure 1 shows the locations of the sampling stations. Stations can be classified into two groups; onshore and offshore. The onshore group includes stations located on the coastal shelf and along transects perpendicular to the coast. A number of these stations were impacted significantly by terrigenous materials from the River Arno plume. The offshore group includes stations located in the Ligurian-Provencal Basin and represent deep, clear oceanic waters that are separated from the coastal zone by a permanent thermal front.

Hydrographic measurements were made using a Seabird SBE 9 CTD system equipped with temperature, conductivity, fluorescence and turbidity sensors. Fluorescence data were calibrated using chlorophyll-*a* concentrations from HPLC measurements, while turbidity data were calibrated using total suspended solids measurements. These were used to generate proxy profiles of *Chl* and *TSS* subsequently used in modelling efforts.

Chlorophyll concentration was measured using standard HPLC measurements on samples filtered through GF/F filters, stored in liquid nitrogen and transported to laboratories for later analysis. *Chl* data presented here were collected by colleagues from Management Unit of the North Sea Mathematical Models (MUMM). Triplicate HPLC samples were analyzed by the Marine Chemistry Laboratory of the MUMM using a reversed phase, acetone-based method with a C18 column and a Jasco FP-1520 fluorescence detector. In this paper *Chl* refers to the chlorophyll *a* concentration and does not include contributions from other pigments.

Total suspended solids concentrations (*TSS*) were obtained by colleagues from MUMM by filtering samples through pre-ashed, rinsed and pre-weighed 47mm GF/F filters. Samples were rinsed with several aliquots of ultrapure water, taking care to rinse the edge of the filter

139 to minimize salt retention. Filters were stored frozen and returned to the lab where they were
140 dried and reweighed.

141 The absorption of all dissolved and suspended components minus water was measured
142 using a Point Source Integrating Cavity Absorption Meter (PSICAM) (Röttgers *et al.* 2005,
143 2007; Röttgers & Doerffer 2007). This instrument has previously been extensively validated
144 and has been shown to provide high accuracy (± 2 %) absorption coefficients across a wide
145 range of water conditions. A 1 m liquid waveguide capillary cell (LWCC) with an Ocean Optics
146 USB2000 mini-spectrometer was used to measure absorption by CDOM. This instrument is
147 somewhat faster to operate than the PSICAM and provides noise range of ± 0.0001 m^{-1} (95%
148 Prediction Interval) at 532 nm. In both cases, measurements were made against fresh Milli-Q
149 references and all samples were corrected for the effects of salinity and temperature on water
150 absorption (Röttgers & Doerffer 2007). From this pair of measurements particulate absorption,
151 $a_p(\lambda)$, was derived by subtraction of CDOM absorption, a_{CDOM}, from PSICAM non-water
152 absorption, a_{PSICAM}.

153 Particulate optical density (OD_p) was measured on freshly filtered samples using a
154 Shimadzu UV-2501 PC dual beam spectrophotometer. Between 1 and 2 litres of sample were
155 filtered through a 25 mm GF/F filter with nominal 0.7 μm retention limit which was mounted
156 directly against the exit port of the spectrophotometer sample chamber. An unused GF/F filter,
157 wetted with 0.2 μm filtered seawater from the same station, was used as a reference sample
158 and mounted on the reference port of the spectrophotometer. After measuring particulate
159 optical density, the sample filter was exposed to a dilute sodium hypochlorite solution until
160 visual loss of pigmentation occurred. The bleached filter pad was rinsed with 0.2 μm filtered
161 seawater before being returned to the sample detector and a further scan for detrital optical
162 density (OD_{det}) was completed. Detrital absorption spectra were visually examined to ensure

that all pigment features, including phycobiliproteins, were removed. The sample was re-bleached and re-scanned if necessary. The absorption coefficient is obtained from

$$a_p(\lambda) = 2.303 \frac{A_{fp} OD_p(\lambda)}{V_v \beta} \quad (1),$$

where A_{fp} is the exposed area of the filter pad, V_f is the volume of sample filtered and β is the pathlength amplification factor. Filter pad absorption spectra were initially baseline corrected at 750 nm (Cleveland and Weidemann 1993). Equation (1) can be rewritten for detrital absorption a_{det} by replacing OD_p with OD_{det}. Samples were corrected for pathlength amplification using a novel procedure described in detail in McKee *et al.* (2014). This approach uses linear regression of filter pad absorption against particulate absorption obtained by subtracting CDOM absorption from total non-water absorption measured by the PSICAM to provide both the pathlength amplification factor and offset correction for each sample. These values were then also used to correct bleached filter pad absorption measurements giving a_{det}, with phytoplankton absorption coefficients, a_{ph}, finally obtained by subtracting detrital absorption from total particulate absorption.

In situ absorption and attenuation measurements were made with an AC-9 absorption and attenuation meter (WET Labs Inc.) with a 25 cm path-length operating at 412, 440, 510, 532, 555, 650, 676 and 715 nm. AC-9 measurements were calibrated during the cruise with ultrapure water (Milli-Q, Millipore) and the salinity and temperature dependence of pure water were corrected in all samples (Pegau *et al.* 1997) using data from a Seabird SBE 19 plus CTD. The *proportional* correction by Zaneveld *et al.* (1994) was used to correct AC-9 absorption data for scattering collection errors. *In situ* backscattering measurements were made with a BB9 backscattering meter (WET Labs Inc.) operating at 412, 440, 510, 532, 595, 660, 676, 715 nm. BB9 data were linearly interpolated where necessary to match AC-9 wavelengths and were corrected for temperature, salinity and path length absorption effects in line with the manufacturer's instructions. The AC-9 and BB9 were deployed simultaneously, measuring

IOPs from the surface to the maximum depth possible in shallow stations or down to a maximum of 100 m for deeper stations.

Radiometric data were collected using a Hyperpro II (Satlantic Inc.) free-falling profiler configured with hyper-spectral radiometric sensors measuring downwelling irradiance (E_d) and upwelling radiance (L_u), with a reference above-surface irradiance (E_s) sensor mounted at an elevated point where the ship's superstructure had minimal effect. The profiling radiometer was deployed in a multicast mode to sample the surface layer repeatedly at each station enabling optimal calculation of light field parameters in the top 10 m (Zibordi *et al.* 2011). In addition, where possible, a deep radiometer cast was collected enabling observation of light penetration below the surface layer. A data processing routine was developed to correct for changes in solar elevation during the cast sequence and to minimize the impact of surface effects (based on Sanjuan Calzado *et al.* 2011).

Underwater light fields were modeled using EcoLight 5.0 (Mobley, Sequoia Scientific) running with IOPs derived from the bio-optical model developed below and Fournier – Forand scattering phase functions generated from particulate backscattering ratio ($b_{bp}(\lambda)/b_p(\lambda)$) following Mobley *et al.* (2002). Output wavelengths and depths were chosen to match AC-9 wavelengths and measured above surface downwards irradiance data were used to set boundary conditions. Raman scattering by water was included in simulations, but due to uncertainty in selection of appropriate quantum yield values, fluorescence contributions from CDOM and phytoplankton were not included in simulations (see Lefering *et al.* 2016 for detailed information).

MERIS above surface remote sensing reflectance data were processed using the Case 2 Region (C2R) algorithm module (Doerffer & Schiller 2007), in Beam-VISAT software (Brockmann Consult). *In situ* data were matched to the geographically closest image pixel for cloud-free images with a maximum one-day shift, before or after.

213

214 **2.2 Bio-optical model development**

215 The Ligurian Sea contains deep, open ocean waters that are broadly consistent with the
216 Case 1 classification where *OSC* are associated with algal production. For these waters it is
217 relatively simple to establish a fairly standard Case 1 bio-optical model with the following
218 form:

219 Case 1 IOP model:

220 $$a(\lambda) = a_w(\lambda) + a_{ph}(\lambda) + {}_{bio}a_{nap}(\lambda) + {}_{bio}a_{cdom}(\lambda) \quad (2)$$

221 $$b(\lambda) = b_w(\lambda) + {}_{bio}b_p(\lambda) \quad (3)$$

222 $$b_b(\lambda) = b_{bw}(\lambda) + {}_{bio}b_{bp}(\lambda) \quad (4),$$

223 where $a(\lambda)$, $b(\lambda)$, and $b_b(\lambda)$ are spectral absorption, scattering and backscattering coefficients.
224 Subscripts *w*, *ph*, *nap* and *CDOM* refer to water, phytoplankton, non-algal particles and
225 coloured dissolved organic material, while the subscript *p* refers to particles. The subscript *bio*
226 has been introduced to emphasise that the Case 1 assumption implies that NAP absorption,
227 CDOM absorption and particulate scattering and backscattering are all assumed to be biogenic
228 in origin and will subsequently be related to the phytoplankton (*Chl*) concentration. Note that
229 the biogenic scattering and backscattering components include all particles present in these
230 waters i.e. phytoplankton and any other associated particles such as biogenic detritus.

231 Coastal waters of the Ligurian Sea are subject to inputs of terrigenous materials from
232 freshwater inflows and resuspension of benthic materials in shallow waters. The following
233 Case 2 bio-optical model is intended to reflect the more complex *OSC* composition of these
234 waters.

235 Case 2 IOP model:

236 $$a(\lambda) = a_w(\lambda) + a_{ph}(\lambda) + {}_{bio}a_{nap}(\lambda) + {}_{nonbio}a_{nap}(\lambda) + {}_{bio}a_{CDOM}(\lambda) + {}_{nonbio}a_{CDOM}(\lambda) \quad (5)$$

$$b(\lambda) = b_w(\lambda) + {}_{bio}b_p(\lambda) + {}_{nonbio}b_p(\lambda) \quad (6)$$

$$b_b(\lambda) = b_{bw}(\lambda) + {}_{bio}b_{bp}(\lambda) + {}_{nonbio}b_{bp}(\lambda) \quad (7).$$

The Case 2 absorption model builds on the Case 1 version by adding nonbiogenic (*nonbio*) NAP particles, effectively an independent sediment fraction, and non-biogenic CDOM absorption, which is intended to reflect freshwater sources of CDOM. Case 2 scattering and backscattering models include additional non-biogenic components, again reflecting contributions, e.g. sediment resuspension, that are independent of the phytoplankton population.

The next step in the model development is to relate each non-water partial IOP to a relevant ecosystem model currency parameter. For the Case 1 model, the relevant ecosystem model currency is *Chl*. There is a wealth of literature on potential Case 1 relationships from which the following were selected having been found to provide reasonable fits with the offshore section of the BP09 data and the global NOMAD data set (Werdell & Bailey 2005). For example, Figure 2 shows the relationship between two wavelengths of phytoplankton absorption and *Chl* and with corresponding modelled values from Bricaud *et al.* (1995) and a more recent parameterisation of the same model by Vellucci, (2007). In this case the Vellucci parameterisation was chosen and has the form

$$a_{ph}(\lambda) = A(\lambda)Chl^{B(\lambda)} \quad (8)$$

Absorption by what is assumed here to be biogenic non-algal particles follows Bricaud *et al.* (1998) and is given by

$${}_{bio}a_{nap}(440) = 0.0124Chl^{0.724} \quad (9)$$

with the spectral dependence given by

$$a_{nap}(\lambda) = {}_{bio}a_{nap}(440)\exp[-0.011(\lambda - 440)] \quad (10).$$

CDOM absorption for Case 1 waters is estimated from Prieur & Sathyendranath (1981)

$${}_{bio}a_{CDOM}(440) = 0.2[a_w(440) + 0.06Chl^{0.65}] \quad (11)$$

and the spectral dependency of CDOM absorption is given by Babin *et al.* (2003)

$$a_{CDOM}(\lambda) = a_{CDOM}(440)\exp\left[-0.017(\lambda - 440)\right] \quad (12).$$

Particulate scattering and backscattering for Case 1 waters are derived from Velluci (2007)

$${}_{bio}b_p(\lambda) = 0.22\left[Chl\right]^{0.612}\left(555/(\lambda)\right) \quad (13)$$

and

$${}_{bio}b_{bp}(\lambda) = A(\lambda)Chl^{B(\lambda)} \quad (14)$$

with $A(\lambda)$ and $B(\lambda)$ coefficients given in Table 5.8 in Velluci (2007). Regression coefficients for modelled *vs* measured IOPs in Case 1 waters are provided in Table 1.

These Case 1 relationships are assumed to hold for the biogenic material found in Case 2 waters. What follows now is an attempt to obtain models for nonbiogenic particulate absorption, scattering and backscattering. In Case 1 waters, *TSS* is assumed to consist of biogenic particles only. A simple regression forced through zero for offshore stations between *TSS* and *Chl* (Figure 4a, R^2=0.29) gives biogenic *TSS* per unit *Chl*:

$$TSS_{bio} = 0.285Chl \quad (15).$$

Eq.16 can be used to estimate the biogenic component of *TSS* in Case 2 waters, with the nonbiogenic *TSS* obtained by subtraction:

$$TSS_{nonbio} = TSS_{Case2} - TSS_{bio} \quad (16).$$

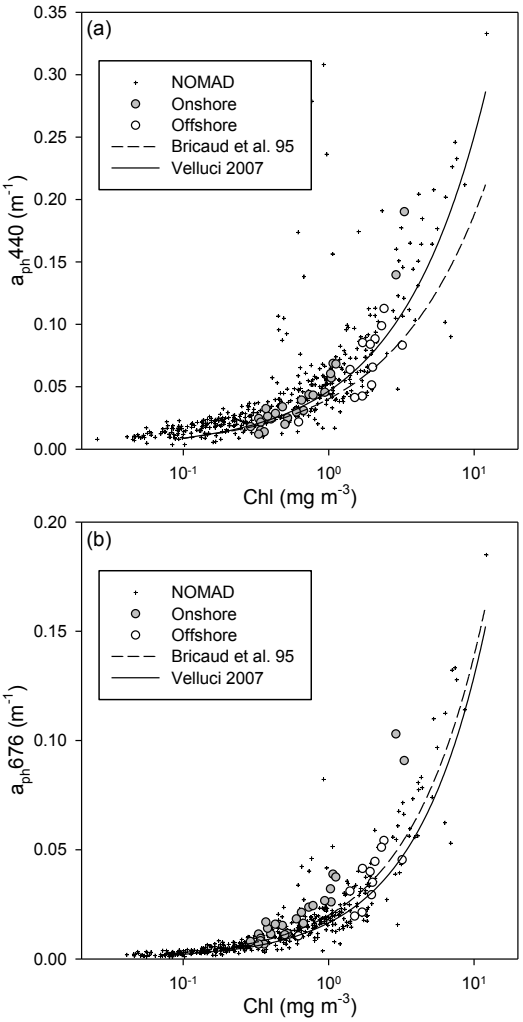

280

281 **Figure 2.** Relationship between a_{ph} and *Chl* at (a) 440 nm and (b) at 676 nm for the NOMAD
282 and Ligurian Sea data sets. The Vellucci (2007) parameterization of the Bricaud *et al.* (1995)
283 model provides an excellent fit to the NOMAD data set over the full spectral range.

284

285 Whilst it is possible to experimentally partition TSS into combustible and non-combustible
286 components, these do not necessarily provide helpful measures for this type of modelling as,
287 for example, the presence of diatom frustules in the non-combustible component potentially
288 breaches the biogenic vs. nonbiogenic partitioning. The TSS partitioning approach presented
289 here is admittedly a little crude, but has the merit of maintaining consistency with the overall
290 model development strategy. For Case 2 waters, the absorption by nonbiogenic particles is

obtained by subtracting ${}_{bio}a_{nap}$ obtained using Eqs. 10 and 11 from measured a_{det}. Likewise, nonbiogenic scattering and backscattering are obtained by subtracting ${}_{bio}b_p$ and ${}_{bio}b_{bp}$ obtained from Eqs. 14 and 15 from observed b_p and b_{bp} for Case 2 stations. Best-fit power law regression of these nonbiogenic partial IOPs against TSS_{nonbio} (Figure 3) gives relationships of the form:

$$ {}_{nonbio}a_{nap}(\lambda) = A_1(\lambda) TSS_{nonbio}^{B_1(\lambda)} \tag{17} $$

$$ {}_{nonbio}b_{p}(\lambda) = A_2(\lambda) TSS_{nonbio}^{B_2(\lambda)} \tag{18} $$

$$ {}_{nonbio}b_{bp}(\lambda) = A_3(\lambda) TSS_{nonbio}^{B_3(\lambda)} \tag{19}. $$

$A_i(\lambda)$ and $B_i(\lambda)$ coefficients for these relationships and their regression coefficients are provided in Table 1.

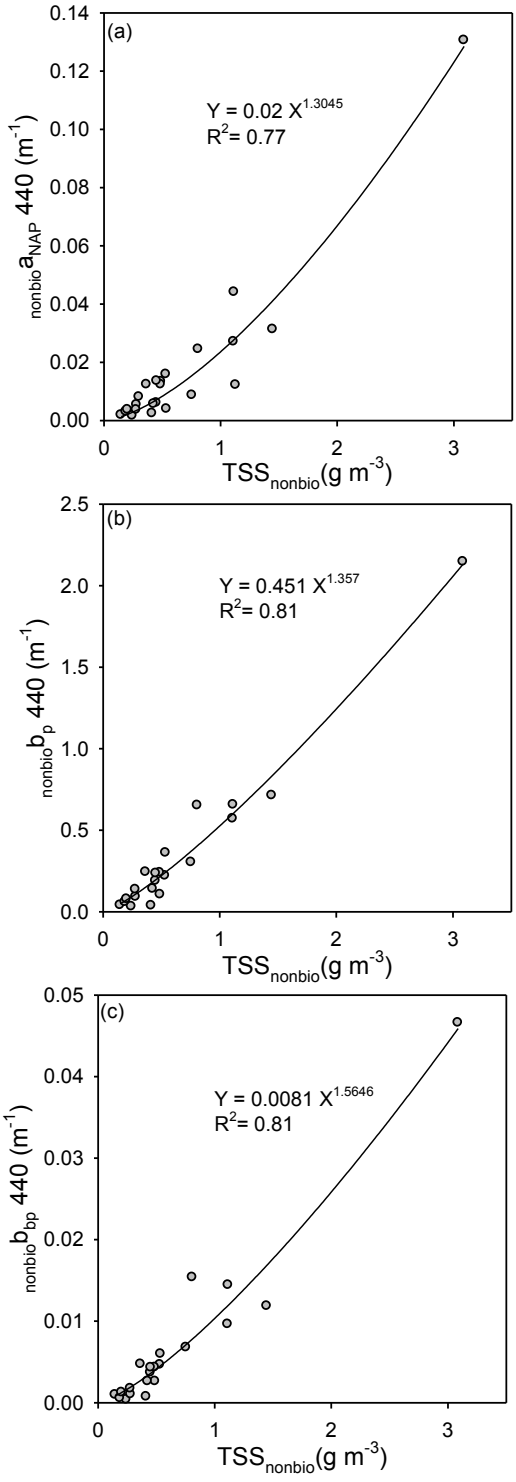

300

301 **Figure 3.** Non-biogenic components of (a) non-algal particulate absorption, (b) particulate
302 scattering and (c) particulate backscattering, all at 440 nm plotted against the non-biogenic
303 component of TSS. Spectrally resolved best-fit parameters are given in Table 1.

304

The final component of the bio-optical model is non-biogenic CDOM absorption, i.e. absorption associated with freshwater inputs into the Ligurian Sea that are not associated with algal properties. Figure 4b shows a global relationship between CDOM absorption and salinity from the NOMAD data set. Low salinity values are associated with regions of stronger freshwater input with higher levels of CDOM absorption. The Mediterranean Sea has very restricted exchange with the global ocean and evaporation rates exceed freshwater inputs leading to unusually high salinity levels, as seen in the relatively high values for the BP09 data included in Figure 4b. As a result, a small offset was added to the global salinity – CDOM relationship for operation in the relatively high salinity waters of the Mediterranean Sea, giving

$$ {}_{nonbio}a_{CDOM}(440) = 0.73 - 0.018 \times Salinity \quad (20). $$

This nonbiogenic component of CDOM absorption is only invoked when salinity drops below a threshold value of 37 PSU, in which case

$$ a_{CDOM}(440) = {}_{bio}a_{CDOM}(440) + {}_{nonbio}a_{CDOM}(440) \quad (21), $$

while the wavelength dependence of CDOM absorption (biogenic and nonbiogenic) is given by Eq. 12.

Table 1. Coefficient values for ${}_{nonbio}a_{nap}(\lambda)$, ${}_{nonbio}b_p(\lambda)$ and ${}_{nonbio}b_{bp}(\lambda)$. Regression coefficients are also presented for biogenic absorption coefficient without water (${}_{bio}a = a_{ph} + {}_{bio}a_{ap} + {}_{bio}a_{CDOM}$), biogenic particulate scattering coefficient (${}_{bio}b_p$) and biogenic particulate backscattering coefficient (${}_{bio}b_{bp}$).

Y Variable	X Variable	Equation	Coefficients	Wavelengths (nm)							
				412	440	488	510	532	555	650	676
${}_{bio}a$	*Chl*	8-12	R^2	**0.84**	**0.84**	**0.83**	**0.8**	**0.78**	**0.72**	**0.78**	**0.82**
${}_{bio}b_p$	*Chl*	13	R^2	**0.72**	**0.71**	**0.71**	**0.71**	**0.71**	**0.71**	**0.68**	**0.67**
${}_{bio}b_{bp}$	*Chl*	14	R^2	**0.42**	**0.41**	**0.43**	**0.43**	**0.45**	**0.47**	**0.46**	**0.53**
${}_{nonbio}a_{nap}$	TSS_{nonbio}	17	A_1 (λ)	0.028	0.02	0.013	0.013	0.011	0.009	0.007	0.002
			B_1 (λ)	1.405	1.3045	1.45	1.49	1.065	1.26	0.87	0.85

			R^2	**0.81**	**0.77**	**0.83**	**0.8**	**0.82**	**0.84**	**0.67**	**0.62**
			A_2 (λ)	0.446	0.451	0.43	0.442	0.4452	0.455	0.435	0.391
$_{nonbio}b_p$	TSS_{nonbio}	**18**	**B_2 (λ)**	1.4167	1.357	1.3135	1.265	1.2566	1.22	1.245	1.342
			R^2	**0.83**	**0.81**	**0.87**	**0.88**	**0.83**	**0.82**	**0.86**	**0.85**
			A_3 (λ)	0.0091	0.0081	0.0087	0.009	0.0081	0.007	0.008	0.006
$_{nonbio}b_{bp}$	TSS_{nonbio}	**19**	**B_3 (λ)**	1.48	1.5646	1.3095	1.264	1.263	1.245	1.416	1.154
			R^2	**0.8**	**0.81**	**0.83**	**0.84**	**0.84**	**0.84**	**0.83**	**0.82**

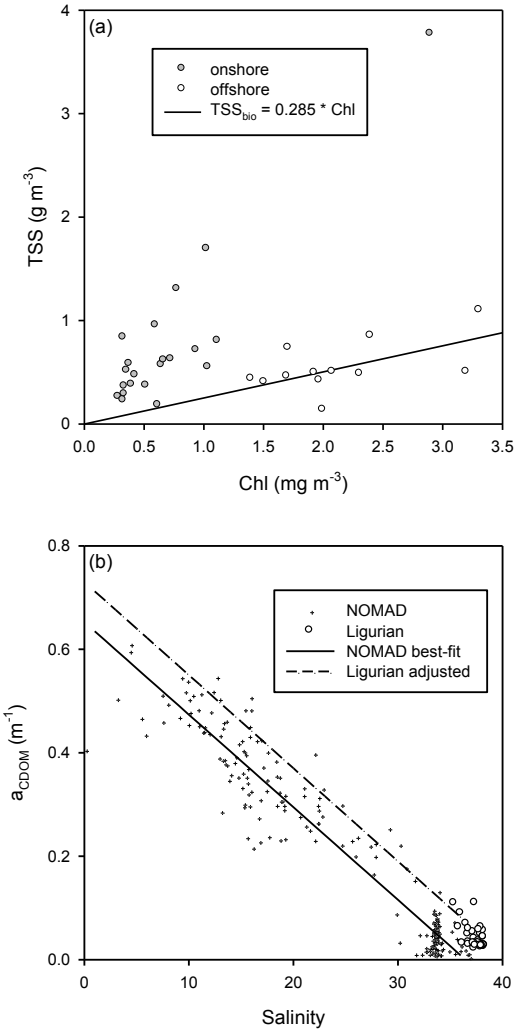

Figure 4 (a) Relationship between *TSS* and *Chl* for onshore and offshore stations. Black line shows the relation between TSS_{ph} and *Chl* for offshore stations (best-fit regression, forced through zero, R^2=0.29). (b) Relationship between $a_{CDOM}(440)$ and salinity measurements for the NOMAD (black circles) and Ligurian Sea (white circles) data sets. The solid line shows

the best fit for the NOMAD data set ($R^2 = 0.91$), and the dashed line shows the offset-adjusted relationship for the Ligurian Sea.

2.2 Bio-optical model validation strategy

The aim of this work is to develop a bio-optical model that will ultimately be incorporated into a Ligurian Sea ecosystem model to improve prediction of underwater light fields and associated impacts on phytoplankton photosynthesis and solar heating. Data for assimilation into and validation of the ecosystem model may ultimately come from a variety of sources including satellite remote sensing and/or *in situ* observations from moorings (static or profiling) or autonomous vehicle platforms (Trees *et al.* 2009). In each case there is a need to adopt common currencies between external data observations and the ecosystem model. In this work, these common currencies have been selected to be *Chl*, *TSS* and *Salinity*. Here simple linear calibrations are applied to turbidity and fluorescence data collected on CTD profiles to generate proxy profiles of *TSS* and *Chl*. Together with a_{CDOM} values derived from *Salinity* profiles, this provides us with an independent set of estimates of OSCs for depths where direct measurements of these parameters were not available. These OSC estimates are then passed into the bio-optical model to generate estimates of partial IOPs for each constituent as depth profiles, and final validation is by comparing estimated total non-water IOPs against directly measured values. By operating on depth profile data, the validation uses thousands of data points for which no OSC measurements were available and IOP data that was not used in the bio-optical model derivation. It also tests the applicability of using simple proxies (Turbidity, Fluorescence and Salinity) to estimate OSCs, including extension into sub-pycnocline and sub-euphotic zone waters where there is a reasonable expectation that such relationships might vary. In this work the data has been partitioned by geographical location, with offshore stations regarded as Case 1 and onshore stations regarded as Case 2. In future it would be possible to

further refine the assignment of Case 1 / 2 status using derived values of *TSS* and *Chl* to determine whether to use Case 1 or Case 2 bio-optical models for the particulate component of IOPs, with the bifurcation in Figure 4a acting as a simple threshold differentiator. Similarly, *Salinity* data reveals whether or not there is a significant freshwater influence and if a nonbiogenic component of CDOM absorption is required.

Validation of the proposed bio-optical model is therefore in four steps (Figure 5):

1. CTD + fluorescence + turbidity profiles provide *Salinity* and estimates of *Chl* and *TSS*.
2. Case 1 or Case 2 bio-optical models are selected as appropriate.
3. Proxy IOP profiles are determined and submitted as input to Ecolight.
4. Modelled radiometric data are compared against *in situ* measurements.

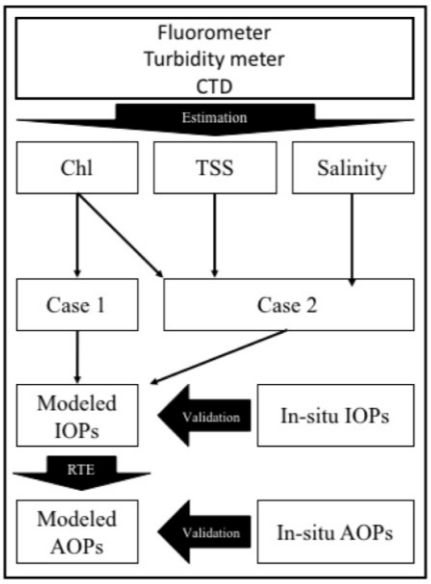

Figure 5. Flow chart for validation of the proposed bio-optical model. NB. This approach extends the validation data set to include thousands of data points that could not be used in model derivation as discrete water samples were limited to a small number of surface stations only.

375 This optical closure approach using *in situ* E_d and L_u data for model validation provides a
376 rigorous test of the bio-optical model and its implementation with a proxy data input method,
377 and therefore gives a relatively strong indication of the level of performance that might be
378 achievable from such a system in practise.
379
380 **3. Results**
381 **3.1 Bio-optical model validation**
382 Turbidity and fluorescence sensors were calibrated with surface *TSS* and *Chl* data from
383 across the region, using data from 35 and 32 stations, respectively. The data ranged between
384 0.29 mg m^{-3} and 3.31 mg m^{-3} for *Chl*, and 0.13 mg l^{-1} and 3.77 mg l^{-1} for *TSS*. Significant linear
385 relationships were found between turbidity values and *TSS* (R^2 = 0.85), and between
386 fluorescence values and *Chl* (R^2 = 0.71). These calibrations were used to generate estimated
387 profiles of *Chl* and *TSS* from CTD fluorescence and turbidity profiles, which, along with CTD
388 *Salinity* profiles, are sufficient to parameterise the Ligurian Sea bio-optical model as described
389 above. The performance of the bio-optical model was determined by comparison with
390 corresponding IOP data obtained from *in situ* AC-9 and BB9 measurements (see Table 2 for
391 descriptive statistics for these measurements). The subsequent performance of Ecolight
392 radiative transfer simulations using the Ligurian Sea bio-optical model as input was assessed
393 against *in situ* radiometric measurements (downwards irradiance E_d and upwards radiance L_u)
394 and derived apparent optical properties (downwards diffuse attenuation coefficient K_d and
395 radiance reflectance R_L). Lefering *et al.* (2016) provides further details of the Ecolight model
396 parameterization used.
397
398 **Table 2.** Descriptive statistics of the *in situ* data from AC-9 and BB9 instruments ($a_{nw} = a_t - a_w$
399 = non-water absorption coefficient, b_p = particulate scattering coefficient, b_{bp} = particulate

backscattering coefficient).

Variable	Parameter	Wavelength (nm)							
		412	440	488	510	532	555	650	676
a_{nw} (m^{-1})	Mean	0.0891	0.0688	0.0410	0.0293	0.0225	0.0140	0.0066	0.0175
	Max	0.6551	0.5402	0.3407	0.2646	0.2050	0.1429	0.0706	0.1606
	Min	0.0013	0.0000	0.0000	0.0000	0.0000	0.0000	0.0000	0.0010
b_p (m^{-1})	Mean	0.4538	0.4402	0.4298	0.4265	0.4201	0.4175	0.3777	0.3513
	Max	3.5746	3.5041	3.3555	3.2637	3.1909	3.1447	2.9598	2.7735
	Min	0.0337	0.0302	0.0292	0.0263	0.0266	0.0259	0.0218	0.0158
b_{bp}(m^{-1})	Mean	0.0086	0.0078	0.0079	0.0084	0.0074	0.0071	0.0069	0.0062
	Max	0.0932	0.0849	0.0837	0.0867	0.0775	0.0747	0.0732	0.0637
	Min	0.0006	0.0006	0.0007	0.0010	0.0008	0.0007	0.0006	0.0005

Retrieved non-water IOPs from the bio-optical model and *in situ* measurements were matched (N= 2047 for absorption and scattering, N=2060 for backscattering) at AC-9 wavelengths (Figure 6 shows data for 440 and 676 nm). Significant correlations (*r*) were observed between model results and *in situ* data for each variable at all wavelengths. The highest correlation, 0.88, was observed for absorption and particulate backscattering at 676 nm, while the lowest correlation, 0.78, was observed for scattering at 676 nm. The range of model error for each IOP is given in Table 3, along with mean and root mean square errors (Eq. 22-23). In each case the range of error is relatively large reflecting the presence of a small number of points that could be described as outliers, but that would, in practice, be part of an input data set. The mean error (Eq. 22) is a useful indicator of model bias, and shows, for example, a tendency for the bio-optical model to over-estimate absorption in the blue. In general, mean error values are low indicating low bias over all. That said, Figure 6 shows that there is a tendency to over-estimate particulate scattering at low values (<0.2 m^{-1}) and underestimate at high values (0.2 – 1 m^{-1}). The root mean square error (RMSE, Eq. 23) provides typical error magnitudes for each parameter. RMSE values vary spectrally from 0.03 to 0.006 m^{-1} for absorption, but are spectrally invariant at ~0.165 m^{-1} and ~0.003 m^{-1} for particulate scattering and backscattering respectively.

$$ME = \frac{\sum_{i=1}^{n}(y_i - y_i')}{n} \quad (22)$$

$$RMSE = \sqrt{\frac{1}{n}\sum_{i=1}^{n}(y_i - y_i')^2} \quad (23)$$

where y and y' are modelled and measured values respectively.

Table 3. Statistical comparison of the *in situ* and modelled IOP data sets.

Statistics	Wavelengths (nm) 412	440	488	510	532	555	650	676
				a_{nw}				
Minimum error	-0.207	-0.140	-0.116	-0.109	-0.099	-0.069	-0.021	-0.064
Maximum error	0.172	0.156	0.094	0.111	0.038	0.046	0.026	0.045
Mean error	0.010	0.015	0.008	0.005	0.002	0.004	0.005	0.001
Root mean square error	0.032	0.029	0.017	0.013	0.009	0.008	0.006	0.007
Linear correlation (r)	0.82	0.84	0.84	0.81	0.82	0.79	0.84	0.88
				b_p				
Minimum error	-2.012	-1.983	-2.064	-2.079	-2.088	-2.101	-2.019	-1.895
Maximum error	2.054	1.698	1.290	1.160	1.177	1.089	1.297	1.575
Mean error	0.013	0.008	-0.017	-0.026	-0.031	-0.037	-0.035	-0.027
Root mean square error	0.163	0.156	0.160	0.164	0.168	0.172	0.166	0.157
Linear correlation (r)	0.83	0.84	0.83	0.82	0.81	0.80	0.78	0.77
				b_{bp}				
Minimum error	-0.056	-0.053	-0.053	-0.055	-0.044	-0.041	-0.045	-0.040
Maximum error	0.038	0.048	0.015	0.010	0.011	0.010	0.029	0.005
Mean error	0.000	0.000	-0.001	-0.002	0.000	0.000	-0.001	-0.001
Root mean square error	0.004	0.003	0.003	0.004	0.003	0.003	0.003	0.002
Linear correlation (r)	0.82	0.79	0.84	0.85	0.84	0.84	0.82	0.87

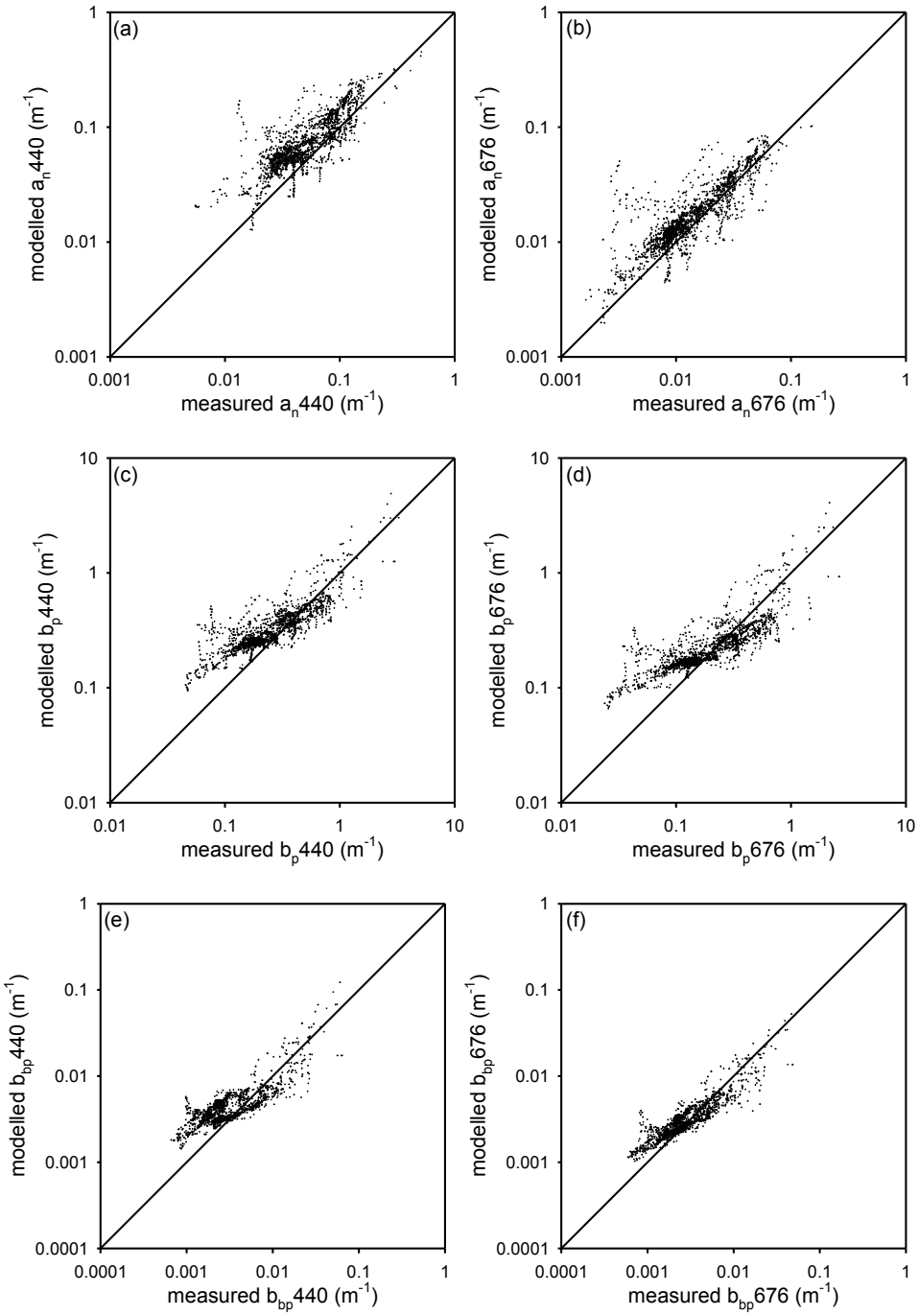

Figure 6. Comparisons of modeled and measured: non-water absorption (a) and (b), particulate scattering (c) and (d), and particulate backscattering (e) and (f) for blue (440 nm) and red (676 nm) wavelengths.

3.2 Radiative transfer model validation

Underwater light fields were simulated for each station using Ecolight (Sequoia Scientific Inc.) parameterised using the bio-optical model described above, together with measured above-surface downwards irradiance values and solar zenith angles. Simulated underwater radiometry outputs were validated against *in situ* spectral E_d and L_u measurements (N = 452) and integrated (400 – 700 nm) photosynthetically available radiation, E_{PAR} and L_{PAR} for all available depths (Figure 7). Correlations between modelled and measured radiometric variables were generally very high (>0.85, Table 4) with E_d generally performing better than L_u. Both E_d and L_u were systematically under-estimated at 676 nm, which is most likely a consequence of not including chlorophyll fluorescence in the radiative transfer simulations. The impact of this bias in the simulation of red wavelength radiometry on PAR estimates is very weak, with both E_{PAR} and L_{PAR} having low bias and RMSE errors. E_{PAR} profiles were used to calculate 1% and 10% light depths (euphotic and mid-euphotic depths respectively, Figure 8). These data showed significant correlations and low errors, with maximum errors of 6 m in euphotic depth, and 8 m in mid-euphotic depth. With RMSE errors of 3.2 m and 2.6 m in euphotic and mid-euphotic depths, respectively, it is clear that the integrated bio-optical / radiative transfer model provides a reasonable representation of the penetration of spectrally averaged sunlight with depth.

Figure 9 shows excellent correlations between measured and modeled radiance reflectance profile data where

$$R_L(\lambda) = L_u(\lambda, z) / E_d(\lambda, z) \quad (24),$$

with the exception of 676 nm where modelled values are significantly lower than measurements, probably due to non-inclusion of algal fluorescence in the simulations. Comparison of modelled surface remote sensing reflectance

$$R_{rs}(\lambda) = L_w(\lambda, 0^+) / E_d(\lambda, 0^+) \quad (25)$$

with MERIS C2R data (Figure 10) also shows strong correlations except for 620 nm, where

456 modelled values are significantly overestimated. In this case, the discrepancy is probably a
457 consequence of inappropriate interpolation of input IOP data (555 and 650 nm are the nearest
458 input wavebands), leading to a poor parameterisation of the radiative transfer model.
459 Comparisons with other satellite data were less convincing, possibly reflecting sensitivity to
460 selection of atmospheric correction scheme and fidelity of match-up conditions.

461

462 **Table 4.** Statistical comparison of *in situ* and modeled radiometry values.

Statistics	Wavelengths (nm)								
	412	**440**	**488**	**510**	**532**	**555**	**650**	**676**	**PAR**
	Ed								
Minimum error	-0.2593	-0.2621	-0.2217	-0.1950	-0.1624	-0.1399	-0.1023	-0.1262	-1.00E+20
Maximum error	0.1770	0.1677	0.2166	0.2038	0.2151	0.2177	0.1417	0.0962	1.00E+20
Mean error	0.0132	0.0083	0.0188	0.0036	-0.0012	-0.0040	-0.0108	-0.0142	-4.67E+17
Root mean square error	0.0673	0.0656	0.0676	0.0552	0.0493	0.0447	0.0280	0.0289	4.74E+19
Linear correlation (r)	0.95	0.97	0.97	0.98	0.98	0.98	0.99	0.98	0.96
	Lu								
Minimum error	-0.0024	-0.0031	-0.0043	-0.0044	-0.0037	-0.0042	-0.0014	-0.0012	-2.00E+18
Maximum error	0.0047	0.0037	0.0021	0.0011	0.0024	0.0020	0.0004	0.0000	1.00E+18
Mean error	0.0005	0.0001	-0.0005	-0.0008	-0.0001	-0.0002	-0.0001	-0.0002	-1.41E+17
Root mean square error	0.0013	0.0010	0.0012	0.0012	0.0009	0.0009	0.0002	0.0002	5.55E+17
Linear correlation (r)	0.92	0.93	0.93	0.95	0.93	0.92	0.91	0.85	0.89

463

464

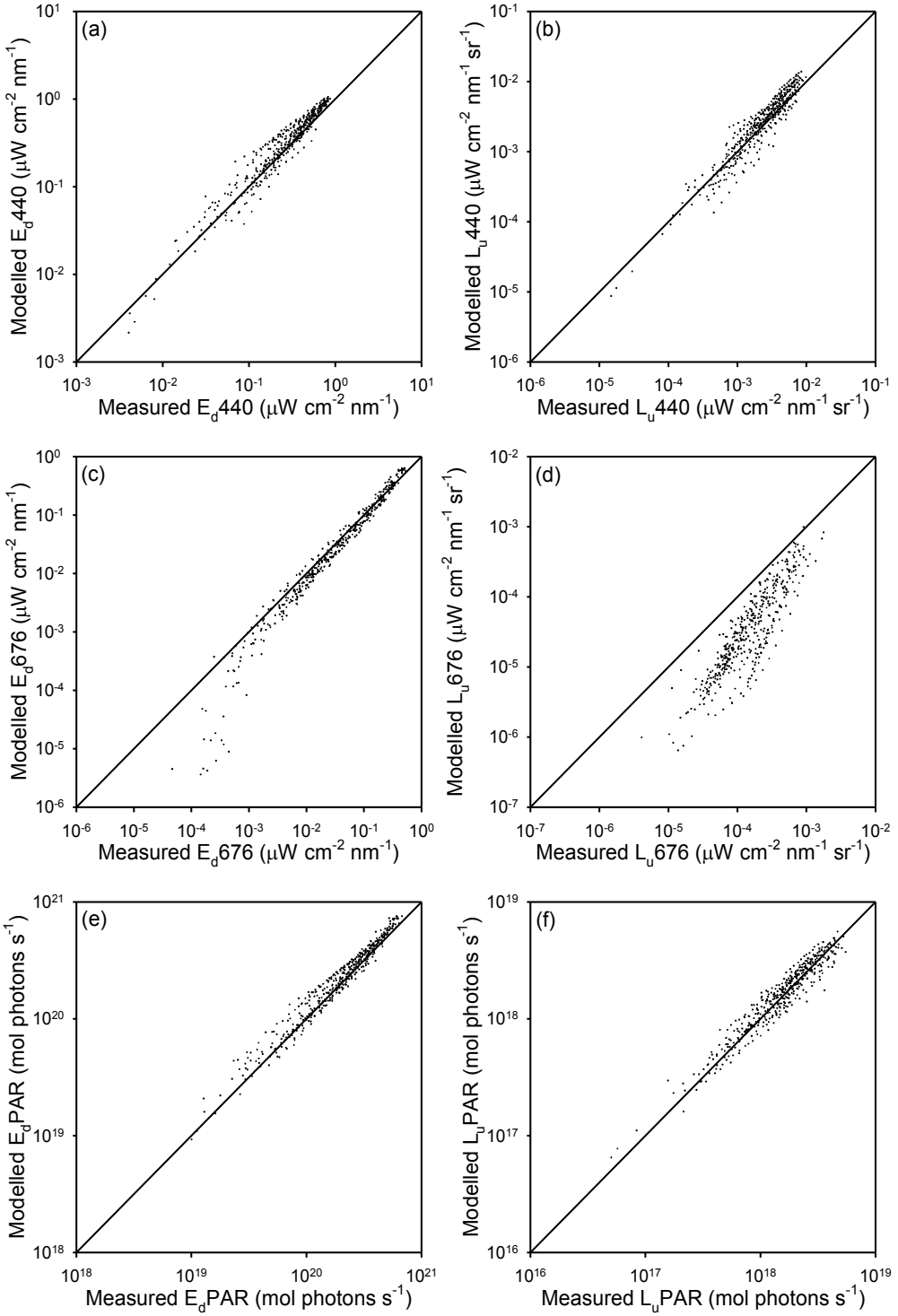

Figure 7. Comparisons of modeled and measured profiles of downwards irradiance, E_d, and upwards radiance, L_u, for blue (440 nm) and red (676 nm) wavelengths, and integrated across the photosynthetically active region, PAR (400 – 700 nm).

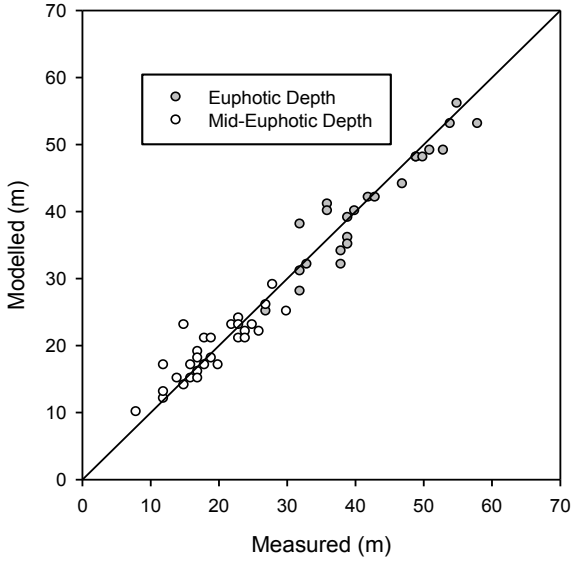

Figure 8. Comparison of modelled and measured euphotic and mid-euphotic depths. NB In-situ radiometry measurements did not always reach the euphotic depth, reducing the number of data points on this plot.

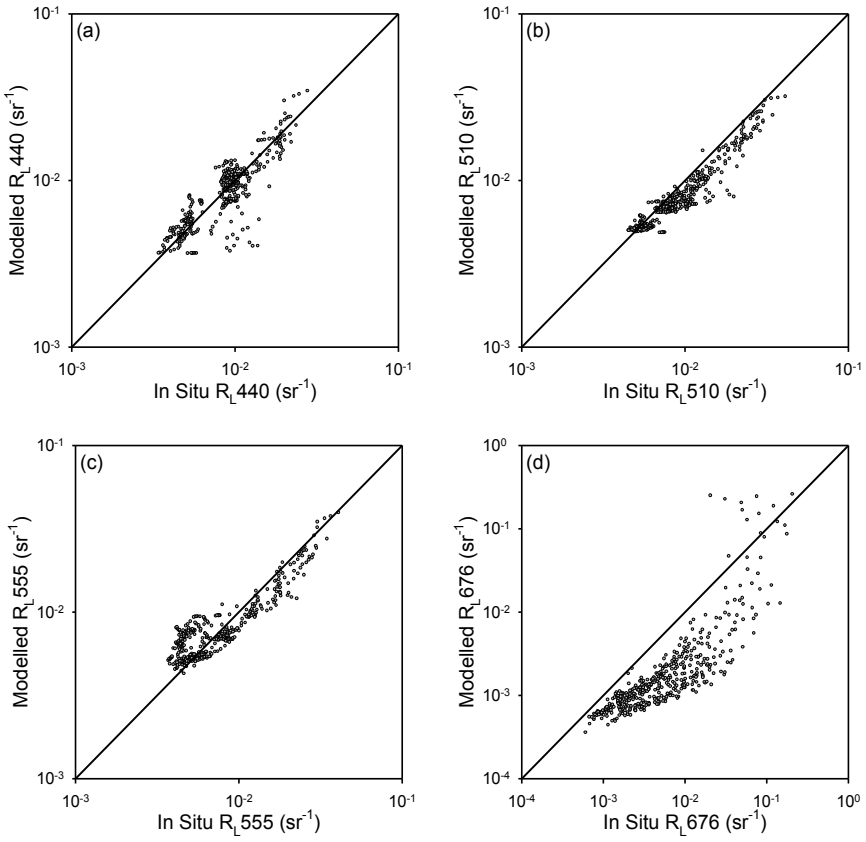

Figure 9. (a-c) Modelled profiles of radiance reflectance generally correlate well with *in situ*

476 measurements in the blue – green. (d) The model under-estimates red radiance reflectance as
477 it does not include the effect of chlorophyll fluorescence.

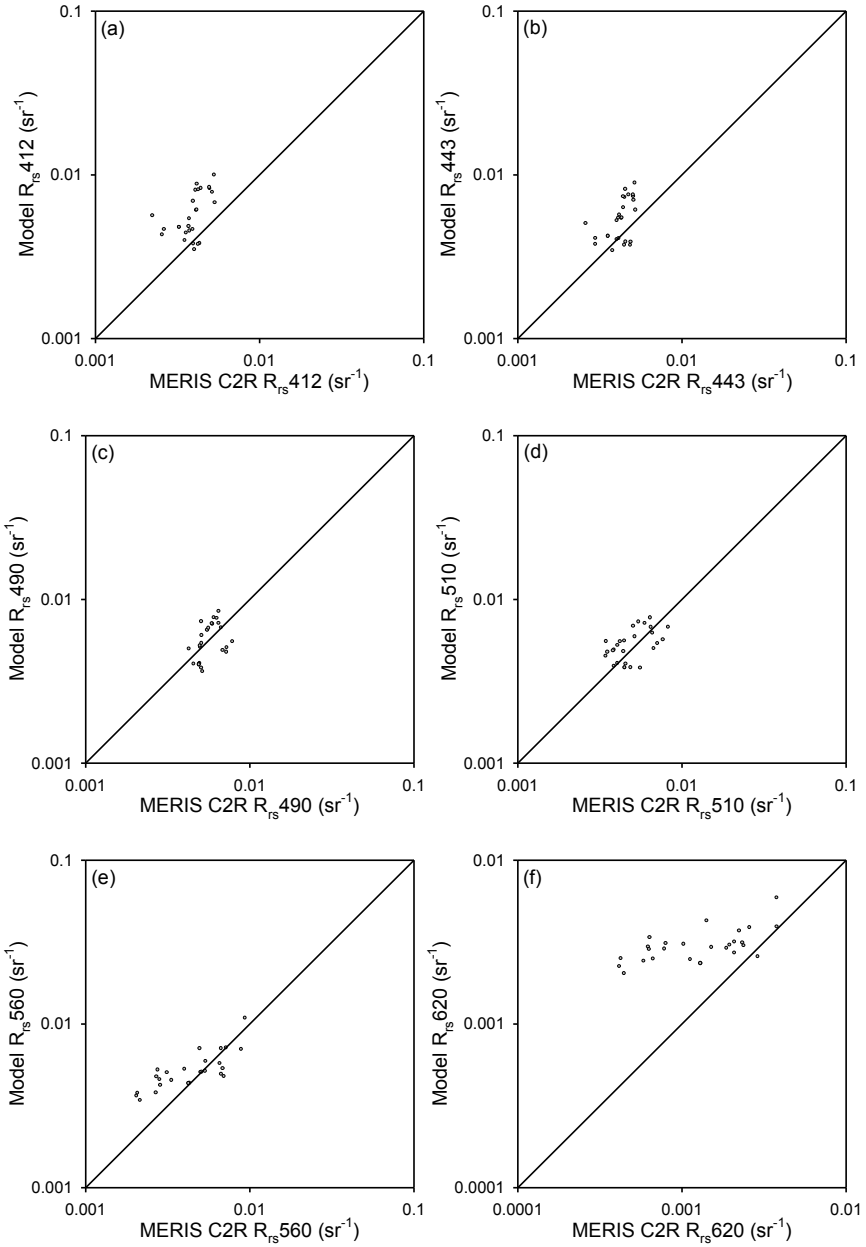

478
479
480 **Figure 10.** (a-e) Modelled above surface remote sensing reflectance corresponds well with
481 MERIS data processed using the C2R algorithm for wavelengths in the blue-green. (f) Model
482 performance is less satisfactory at 620 nm, potentially as a result of inadequate interpolation of
483 input data to the model (555 and 650 nm the nearest input wavebands). NB. Includes data from
484 both onshore and offshore stations.

4. Discussion and Conclusion

The integrated Case 1 and Case 2 Ligurian Sea bio-optical model developed here has been shown to provide an effective characterization of the optical properties of the region. In doing so, it is worth considering the various stages of model development that have been incorporated into the validation scheme. Although the Case 1 elements of the bio-optical model are relatively standard, the Case 2 section contains several innovations including statistical partitioning of *TSS* and derivation of partial IOPs for non-biogenic particles. It also includes a separation of CDOM contributions from biogenic (effectively phytoplankton) and non-biogenic (freshwater) sources. A scheme for partitioning the region into Case 1, Case 2 (non-biogenic particles) and Case 2 (freshwater influence) zones based on *Chl*, *TSS* and *Salinity* values has been presented which is essential for correctly selecting the appropriate bio-optical model for any given point in space. It is also worth emphasizing that the performance of the model has been demonstrated using proxy values of *Chl* and *TSS* derived from *in situ* fluorescence and turbidity measurements, which introduces another set of measurement uncertainties into the analysis. The resulting comparisons with *in situ* IOP data are therefore particularly encouraging given this added layer of data manipulation.

Our approach aims to use the bio-optical model to convert easily measured proxies (in in this case Salinity, Fluorescence and Turbidity from CTD profiles) into IOP profiles and ultimately allow estimation of spectral remote sensing reflectance. There are two crucial early steps that need to be treated with due caution: (1) conversion of these simple proxies into OSC concentrations, and (2) selection of Case 1 or Case 2 bio-optical models for any given data point. There is considerable scope for further refinement of both steps beyond the very simple approach adopted here. For example, there are many potential options for partitioning water masses using combinations of IOP, constituent data and other physical variables (McKee and

510 Cunningham 2006, Chang *et al.* 2006).

511 The utility of this bio-optical model for predicting underwater and water-leaving light
512 fields has been tested through rigorous optical closure analysis against *in situ* and remotely
513 sensed radiometry and AOPs. When considering the level of performance achieved, it should
514 be recognized that direct optical closure between *in situ* IOPs and radiometry remains elusive
515 and rarely demonstrated to date (Tzortziou *et al.* 2006). The degree of closure demonstrated
516 here is therefore very encouraging and suggests that major features of the optical characteristics
517 of the region have been satisfactorily captured in the bio-optical model.

518

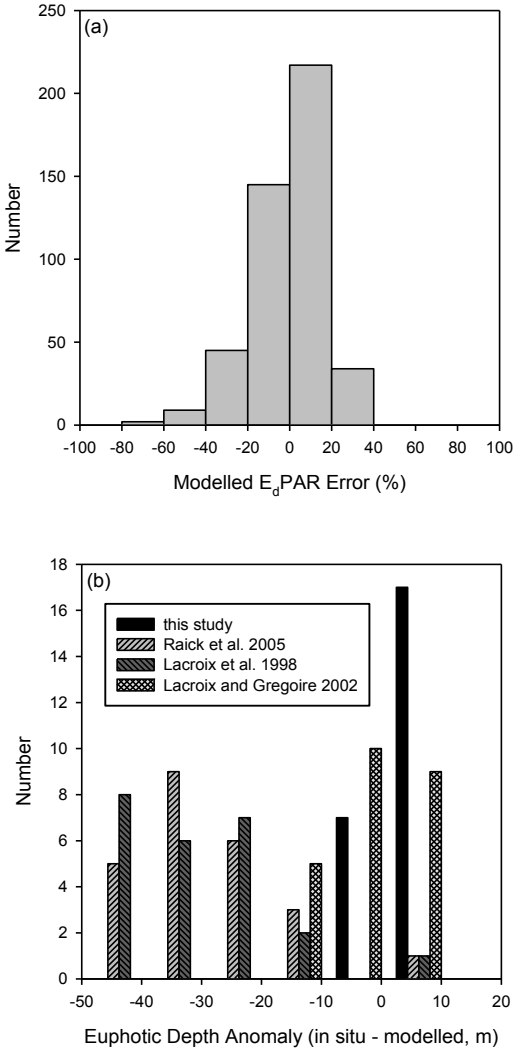

519
520
521 **Figure 11.** (a)Percentage error of modeled $E_d\,PAR$ values using approach presented

here. (b) Anomaly of modelled euphotic depths for the approach developed here and previous studies.

A major motivation for this work is to develop a bio-optical model that can be incorporated into radiative transfer simulations to provide accurate predictions of underwater photosynthetically available radiation. Figure 11a shows the distribution of percentage errors in modeled PAR (E_d) across all available stations and depths for this data set, with 80% of points falling within ±20% and a 95 % prediction interval of ±33%. Predictions of euphotic depth from the approach developed here compare favourably (Figure 11b) against values calculated from previous approaches of Lacroix & Nival 1998, and Raick *et al.* 2005 which do not account for non-algal contributions. The Lacroix & Gregoire (2002) model is closer in performance to the model developed here, benefitting from a slightly more representative underwater light field model than the earlier study. However, analysis of performance separating into onshore and offshore groups (Figure 12) highlights the benefit of directly accounting for both non-biogenic particles and freshwater sources of CDOM for modeling euphotic depth in optically complex onshore stations.

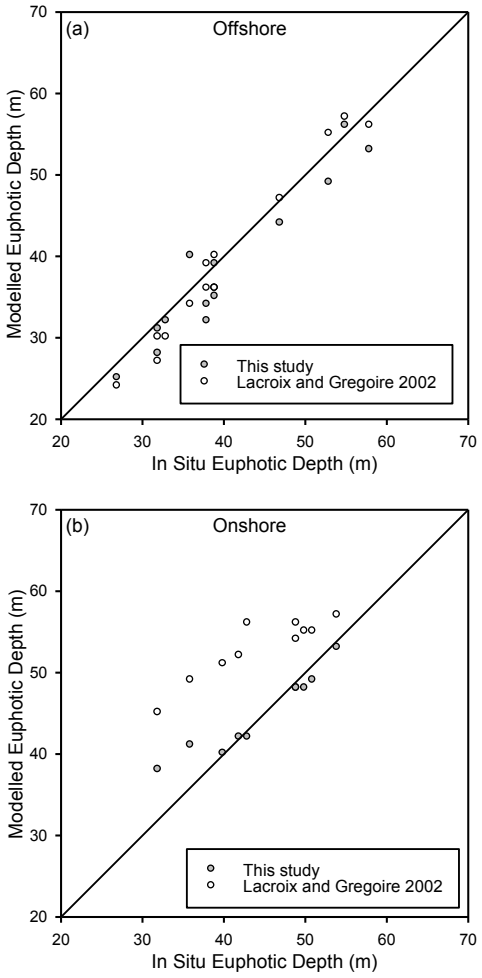

Figure 12. (a) Euphotic depth is modelled for offshore waters with similar accuracy by the model presented here and the previous model by Lacroix and Gregoire (2002). (b) The Lacroix and Gregoire (2002) model over-estimates euphotic depth for optically complex on shore waters. The model presented here performs better in these waters as it captures the effect of non-algal materials as well as phytoplankton.

The Ligurian Sea bio-optical model developed here has been specifically designed to be able to accommodate a wide variety of potential data sources and to integrate into ecosystem models with minimal need for adaptation. Generating estimates of *Chl*, *TSS* and *Salinity* from *in situ* data is reasonably straightforward, though there is obviously scope for complications under some circumstances e.g. strong differences in fluorescence: *Chl* can occur under light, nutrient or species composition gradients. Nonetheless, the performance of the model across

550 the wide range of conditions encountered in this data set suggests that such effects may not be
551 fatal to performance under reasonably common circumstances.
552 OCRS is a potentially important data source for assimilation and validation of coupled
553 physical-ecosystem models, with optical closure against measured reflectance data, such as is
554 demonstrated here, being a useful tool for tracking model performance. Chang et al. (2006)
555 have shown how it might be possible to use reflectance spectra for further refinement of water
556 masses. However, caution is required in the interpretation of OCRS standard products in
557 optically complex waters. An example of where due caution is required is illustrated in Figure
558 1. Standard OCRS *Chl* products based on blue-green reflectance ratios tend to perform poorly
559 in turbid coastal waters (e.g. McKee *et al.* 2007), with high sediment levels resulting in the
560 return of over-estimates of *Chl*. This is most likely the case with the Arno plume seen in the
561 centre of Figures 1 (c and d). It would be essential to establish the performance of OCRS
562 algorithms in the region of interest before using such data to estimate *Chl* and *TSS*. Obtaining
563 *Salinity* from space is even more challenging, with sensors such as the now-defunct Aquarius
564 offering much lower resolution than would be required to resolve important features such as
565 the Arno plume that features strongly in this area. Direct estimation of CDOM absorption from
566 ocean colour remote sensing, if available, would provide a welcome alternative data source for
567 this kind of application. Whilst ocean colour CDOM products are available, it is not clear that
568 they are able to achieve the level of discrimination between dissolved CDOM and detrital
569 particulate absorption that is necessary for this application. This is an area that requires further
570 development at this time. On the modeling side, both *Chl* and *Salinity* are commonly used
571 model currencies that fit seamlessly with the bio-optical model for the Ligurian Sea. However,
572 the non-biogenic *TSS* component requires inclusion of benthic resuspension and lateral
573 transport of mineral particles to be included in the coupled physical-ecosystem model (Everett
574 *et al.* 2007, Sheng and Kim 2009). This feature is not included by default in many such models

575 and introduction of these processes would potentially impact on computation time and would
576 require specific validation. However, given the influence on euphotic depth and light
577 availability for photosynthesis, and the impact on remote sensing reflectance signals that are
578 often proposed for model assimilation and validation schemes, it seems clear that modeling
579 mineral particle transport and dispersal is a necessary step for shallow coastal waters. This
580 work strongly points towards this being an important area for coastal and shelf sea model
581 development.

582 The next logical step in this work is to attempt to incorporate a radiative transfer model
583 using the bio-optical relationships established here into a coupled physical-ecosystem model
584 for the Ligurian Sea and compare performance with and without (a) any light field model, (b)
585 a Case 1 only bio-optical model, and (c) the integrated Case 1 and Case 2 bio-optical model
586 (Mobley *et al.* 2015). As well as directly impacting on phytoplankton productivity estimates,
587 there is scope to influence solar heating of the water column with potential impacts on
588 stratification and possibly circulation in some cases (Murtugudde *et al.* 2002). Further efforts
589 along this line of research are planned.

590

591 **5. Acknowledgements**

592 This work was supported by the OSS2015 EU 7th Framework Project, CMRE NATO
593 visiting researcher program (Bengil), British Council travel grant (Bengil) and award of a
594 NERC Advanced Fellowship (NE/E013678/1 - McKee). We would like to thank the captain
595 and crew of *NR/V Alliance* for their assistance during data collection at sea. We would also like
596 to thank collaborators from the BP09 cruise who kindly provided access to ancillary data sets.
597 Comments from Grace Chang and two anonymous reviewers were very gratefully received.

598

599 **6. References**

600 Astraldi, M., Gasparini, G.P., 1992. The Seasonal Characteristics of the Circulation in the
601 North Mediterranean Basin and Their Relationship with the Atmospheric-Climatic
602 Conditions. J. Earth Syst. Sci. 97, 9531–9540.

603 Astraldi, M., Gasparini, G.P., Manzella, G.M.R., Hopkins, T.S., 1990. Temporal Variability of
604 Currents in the Eastern Ligurian Sea. J. Geophys. Res. 95, 1515–1522.

605 Babin, Marcel; Stramski Dariusz, Ferrari M. Giovanni, Claustre Herve, Bricaud Annick,
606 Obolensky Grigor, H.N., Babin, M., Stramski, D., Ferrari, G.M., Claustre, H., Bricaud,
607 A., Obolensky, G., Hoepffner, N., 2003. Variations in the light absorption coefficients of
608 phytoplankton, nonalgal particles, and dissolved organic matter in coastal waters around
609 Europe. J. Geophys. Res. 108, 4.1–4.20. doi:10.1029/2001JC000882

610 Beşiktepe, Ş., T., Lermusiaux, P.F.J., Robinson, A.R., 2003. Coupled physical and
611 biogeochemical data-driven simulations of Massachusetts Bay in late summer: Real-time
612 and postcruise data assimilation. J. Mar. Syst. 40-41, 171–212. doi:10.1016/S0924-
613 7963(03)00018-6

614 Bowers, D.G., Harker, G.E.L., Smith, P.S.D., Tett, P., 2000. Optical properties of a region of
615 freshwater influence (The Clyde Sea). Estuar. Coast. Shelf Sci. 50, 717–726.

616 Bricaud, A., Morel, A., Babin, M., Allali, K., Claustre, H., 1998. Variations of light absorption
617 by suspended particles with chlorophyll a concentration in oceanic (case 1) waters:
618 Analysis and implications of r bio-optical models. J. Geophys. Res. 103, 31033–31044.

619 Bricaud, A., Roesler, C., Zaneveld, J.R. V., 1995. In situ methods for measuring the inherent
620 optical properties of ocean waters. Limnol. Oceanogr. 40, 393–410.
621 doi:10.4319/lo.1995.40.2.0393

622 Chang, G.C., Barnard, A. H., McLean, S., Egli, P.J., Moore, C., Zaneveld, J.R.V., Dickey, T.D.,
623 Hanson, A., 2006. In situ optical variability and relationships in the Santa Barbara
624 Channel: implications for remote sensing, Appl. Opt., 45, 3593-3604.
625 Ciavatta, S., Torres, R., Martinez-Vicente, V., Smyth, T., Olmo, G.D., Polimene, L., Allen, J.
626 I., 2014. Assimilation of remotely-sensed optical properties to improve marine
627 biogeochemistry modelling. Prog. Oceanogr. 127, 74–95.
628 Cleveland, J.S., Weidemann, A.D., 1993. Quantifying absorption by aquatic particles: A
629 multiple scattering correction for glass-fiber filters. Limnol. Oceanogr. 38, 1321–1327.
630 doi:10.4319/lo.1993.38.6.1321
631 Dickey, T., Lewis, M., Chang, G., 2006. Optical oceanography: recent advances and future
632 directions using global remote sensing and in situ observations. Rev. Geophys. 44, 1–39.
633 doi:10.1029/2003RG000148.1
634 Dickey, T.D., Falkowski, P.G., 2002. Solar energy and its biological – physical interactions in
635 the sea, The Sea. John Wiley & Sons, Inc., New York.
636 Doerffer, R., Schiller, H., 2007. Measurements of optical absorption by chromophoric
637 dissolved organic matter using a point-source integrating-cavity absorption meter. Int. J.
638 Remote Sens. 28, 517–535.
639 Everett, J.D., Baird, M.E., Suthers, I.M., 2007. Nutrient and plankton dynamics in an
640 intermittently closed/open lagoon, Smiths Lake, south-eastern Australia: An ecological
641 model. Estuar. Coast. Shelf Sci. 72, 690–702. doi:10.1016/j.ecss.2006.12.001
642 Fujii, M., Boss, E., Chai, F., 2007. The value of adding optics to ecosystem models : a case
643 study. Biogeoscience 4, 817–835.
644 Gordon, H.R., Morel, A., 1981. Water Colour Measurements - An Introduction. Mar. Sci. 13,
645 207–212.

646 Klemas, V., Borchardt, J.F., Treasure, W.M., 1973. Suspended sediments observations from
647 ERTS-1. Remote Sens. Environ. 2, 205–221.
648 Lacroix, G., Gregoire, M., 2002. Revisited ecosystem model (MODECOGeL) of the Ligurian
649 Sea: seasonal and interannual variability due to atmospheric forcing. J. Mar. Syst. 37,
650 229–258. doi:http://dx.doi.org/10.1016/S0924-7963(02)00190-2
651 Lacroix, G., Nival, P., 1998. Influence of meteorological variability on primary production
652 dynamics in the Ligurian Sea (NW Mediterranean Sea) with a 1D
653 hydrodynamic/biological model. J. Mar. Syst. 16, 23–50. doi:10.1016/S0924-
654 7963(97)00098-5
655 Lee, Z.P., Du, K.P., Arnone, R., Liew, S.C., Penta, B., 2005. Penetration of solar radiation in
656 the upper ocean: A numerical model for oceanic and coastal waters. Journal of
657 Geophysical Research C: Oceans, 110 (9), art. no. C09019, pp. 1-12.
658 doi:10.1029/2004JC002780
659 Lefering, I., Bengil, F., Trees, C., Röttgers, R., Bowers, D., Nimmo-Smith, W.A.M, Schwarz,
660 J., McKee, D. 2016. Optical closure in marine waters from in situ inherent optical property
661 measurements. Opt. Expr. 24, 14036-14052.
662 Loisel, H., Morel, A., 1998. Light scattering and chlorophyll concentration in case 1 waters: A
663 reexamination. Limnol. Oceanogr. 43, 847–858. doi:10.4319/lo.1998.43.5.0847
664 Marty, J.C., Chiavérini, J., Pizay, M.D., Avril, B., 2002. Seasonal and interannual dynamics of
665 nutrients and phytoplankton pigments in the western Mediterranean Sea at the
666 DYFAMED time-series station (1991-1999). Deep. Res. Part II Top. Stud. Oceanogr. 49,
667 1965–1985. doi:10.1016/S0967-0645(02)00022-X
668 McKee, D., Röttgers, R., Neukermans, G., Calzado, V.S., Trees, C., Ampolo-Rella, M., Neil,
669 C., Cunningham, A., 2014. Impact of measurement uncertainties on determination of

670 Chlorophyll-specific absorption coefficient for marine phytoplankton. Geophys. Res.
671 Ocean. 119, 9013–9025.
672 Mobley, C.D., Chai, F., Xiu, P., Sundman, L.K., 2015. Impact of improved light calculations
673 on predicted phytoplankton growth and heating in an idealized upwelling-downwelling
674 channel geometry. J. Geophys. Res. Ocean. 120, 875–892. doi:10.1002/2014JC010588
675 Mobley, C.D., Sundman, L.K., Boss, E., 2002. Phase function effects on oceanic light fields.
676 Appl. Opt. 41, 1035. doi:10.1364/AO.41.001035
677 Morel, A., Maritorena, S., 2001. Bio-optical properties of oceanic waters : A reappraisal. J.
678 Geophys. Res. 106, 7163–7180.
679 Morel, A., 2009. Are the empirical relationships describing the bio-optical properties of case 1
680 waters consistent and internally compatible? J. Geophys. Res. Ocean. 114, 1–15.
681 doi:10.1029/2008JC004803
682 Morel, A., 1988. Optical Modeling of the Upper Ocean in Relation to Its Biogenous Matter
683 Content (Case I Waters). J. Geophys. Res. 93, C9, 10749 – 10768.
684 Murtugudde, R., Beauchamp, J., McClain, C.R., Lewis, M., Busalacchi, A.J., 2002. Effects of
685 penetrative radiation on the upper tropical ocean circulation. J. Clim. 15, 470–486.
686 Pegau, W., Gray, D., Zaneveld, J., 1997. Absorption and attenuation of visible and near-
687 infrared light in water: dependence on temperature and salinity. Appl. Opt. 36, 6035–
688 6046.
689 Penta, B., Lee, Z., Kudela, R.M., Palacios, S.L., Gray, D.J., Jolliff, J.K., Shulman, I.G., 2008.
690 An underwater light attenuation scheme for marine ecosystem models. Opt. Expr. 16 (21),
691 16581-16591.
692 Penta, B., Lee, Z., Kudela, R.M., Palacios, S.L., Gray, D.J., Jolliff, J.K., Shulman, I.G., 2009.
693 An underwater light attenuation scheme for marine ecosystem models: errata. Opt. Expr.
694 17 (25), 23351.

695 Picco, P., Cappelletti, a., Sparnocchia, S., Schiano, M.E., Pensieri, S., Bozzano, R., 2010.
696 Upper layer current variability in the Central Ligurian Sea. Ocean Sci. 6, 825–836.
697 doi:10.5194/os-6-825-2010
698 Prieur, L., Sathyendranath, S., 1981. An Optical Classification of Coastal and Oceanic Waters
699 Based on the Specific Spectral Absorption Curves of Phytoplankton Pigments, Dissolved
700 Organic Matter, and Other Particulate Materials. Limnol. Oceanogr. 26, 671–689.
701 doi:10.2307/2836033
702 Raick, C., Delhez, E.J.M., Soetaert, K., Grégoire, M., 2005. Study of the seasonal cycle of the
703 biogeochemical processes in the Ligurian Sea using a 1D interdisciplinary model. J. Mar.
704 Syst. 55, 177–203. doi:10.1016/j.jmarsys.2004.09.005
705 Rothstein, L., Cullen, J., Abbott, M., Chassignet, E., Denman, K., Doney, S., Ducklow, H.,
706 Fennel, K., Follows, M., Haidvogel, D., Hofmann, E., Karl, D., Kindle, J., Lima, I.,
707 Maltrud, M., McClain, C., McGillicuddy, D., Olascoaga, M.J., Spitz, Y., Wiggert, J.,
708 Yoder, J., 2006. Modeling Ocean Ecosystems: The PARADIGM Program. Oceanography
709 19, 22–51. doi:10.5670/oceanog.2006.89
710 Röttgers, R., Doerffer, R., 2007. Measurements of optical absorption by chromophoric
711 dissolved organic matter using a point-source integrating-cavity absorption meter.
712 Limnol. Oceanogr. Methods 5, 126–135.
713 Röttgers, R., Schönfeld, W., Kipp, P.-R., Doerffer, R., 2005. Practical test of a point-source
714 integrating cavity absorption meter: the performance of different collector assemblies.
715 Appl. Opt. 44, 5549–5560.
716 Röttgers, R., Häse, C., Doerffer, R., 2007. Determination of the particulate absorption of
717 microalgae using a point-source integrating-cavity absorption meter: verification with a
718 photometric technique, improvements for pigment bleaching, and correction for
719 chlorophyll fluorescence. Limnol. Oceanogr. Methods 5, 1–12. doi:10.4319/lom.2007.5.1

720 Sanjuan Calzado, V., 2009. Bio-optical modeling for ecosystems in case II waters. Univ.
721 Southampton, Sch. Ocean Earth Sci.
722 Sheng, Y.P., Kim, T., 2009. Skill assessment of an integrated modeling system for shallow
723 coastal and estuarine ecosystems. J. Mar. Syst. 76, 212–243.
724 doi:10.1016/j.jmarsys.2008.05.011
725 Shulman, I., Frolov, S., Anderson, S., Penta, B., Gould, R., Sakalaukus, P., Ladner, S., 2013.
726 Impact of bio-optical data assimilation on short-term coupled physical, bio-optical model
727 predictions. J. Geophys. Res. Ocean. 118, 2215–2230. doi:10.1002/jgrc.20177
728 Trees, C., Sanjuan Calzado, V., Besiktepe, S., McKee, D., Bengil, F., Gunduz, M.,
729 Twardowski, M., 2012. Optical physical and ecosystem regional modeling Assessment
730 (OPERA): A revolutionary Approach, in Ocean Optics XXI. Glasgow.
731 Tzortziou, M., Herman, J.R., Gallegos, C.L., Neale, P.J., Subramaniam, A., Harding, L.W.,
732 Ahmad, Z., 2006. Bio-optics of the Chesapeake Bay from measurements and radiative
733 transfer closure. Estuar. Coast. Shelf Sci. 68, 348–362. doi:10.1016/j.ecss.2006.02.016
734 Vellucci, V., 2007. Optical properties in the Mediterranean open waters. PhD Thesis from
735 Università Degli Studi Di Napoli “Federico II”.
736 Werdell, P.J., Bailey, S.W., 2005. An improved in-situ bio-optical data set for ocean color
737 algorithm development and satellite data product validation. Remote Sens. Environ. 98,
738 122–140.
739 Zaneveld, J.R. V., Kitchen, J.C., Moore, C., 1994. The scattering Error Correction of
740 Reflecting-Tube Absorption Meters. Ocean Opt. XII. Int. Soc. Opt. Photonics.
741 doi:10.1117/12.190095
742 Zibordi, G., Berthon, J.F., Melin, F., D’Alimonte, D., 2011. Cross-site consistent in situ
743 measurements for satellite ocean color applications: The BiOMaP radiometric dataset.
744 Remote Sens. Environ. 15, 2104–2115.